ACS APPLIED MATERIALS & INTERFACES

Research Article

www.acsami.org

Green Synthesis of Large-Scale Highly Ordered Core@Shell Nanoporous Au@Ag Nanorod Arrays as Sensitive and Reproducible 3D SERS Substrates

Bin Chen,[†] Guowen Meng,*[,†,‡] Qing Huang,[§] Zhulin Huang,[†] Qiaoling Xu,[†] Chuhong Zhu,[†] Yiwu Qian,[†] and Yi Ding[∥]

[†]Key Laboratory of Materials Physics and Anhui Key Laboratory of Nanomaterials and Nanostructures, Institute of Solid State Physics, Chinese Academy of Sciences, Hefei 230031, China

[‡]University of Science and Technology of China, Hefei 230026, China

[§]Key Laboratory of Ion Beam Bioengineering, Chinese Academy of Sciences, Hefei 230031, China

[∥]School of Chemistry and Chemical Engineering, Shandong University, Jinan 250100, China

Supporting Information

ABSTRACT: We present a simple green synthetic approach to large-scale and highly ordered arrays of vertical nanoporous Au nanorods, with an ultrathin Ag-layer in situ electrodeposited on each nanoporous Au nanorod (denoted as core@shell nanoporous Au@Ag nanorod). As both the nanopores within each nanorod and the gaps between the neighboring nanorods create three-dimensional (3D) "hot spots" homogeneously distributed throughout the whole substrate, the core@shell nanoporous Au@Ag nanorod arrays were proved to be sensitive and reproducible surface-enhanced Raman scattering (SERS) substrates. Not only universal probe molecules (rhodamine 6G, R6G) but also nonadsorbing molecules (polychlorinated biphenyls, PCBs) have been detected by using the substrates. After mono-6-thio-β-cyclodextrin (HS-β-CD) was modified to efficiently capture more PCBs molecules, the detection limit of PCBs was further reduced to 5.35×10^{-7} M. As a trial of practical application, R6G and PCBs with different molar ratios in their mixed solutions were identified, and two congeners of PCBs in their mixture could also be distinguished, showing great potentials in real-time simultaneous detection of multiple pollutants.

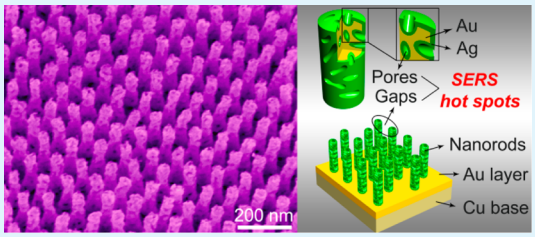

KEYWORDS: *nanoporous nanorod arrays, core@shell, green synthesis, surface-enhanced Raman scattering, large-scale uniform substrates, rapid detection*

1. INTRODUCTION

Surface-enhanced Raman scattering (SERS) has been recognized as a powerful spectroscopic tool for rapid identification of analytes with high sensitivity and fingerprint character.[1] It has been demonstrated that the SERS sensitivity depends strongly on the electromagnetic (EM) field enhancement induced from the localized surface plasmon resonances (LSPR) at interstitial junctions or nanogaps between the plasmonic nanostructures, also known as hot spots.[2] For practical applications, it is desired for an effective SERS substrate to possess not only enormous hot spots to ensure high sensitivity but also uniform distribution of the hot spots to achieve good signal reproducibility and should be simple and green to prepare.[3] To date, considerable effort has been devoted to the building of various nanostructures,[4] such as nanospheres,[5] nanorods,[6] nanocubes,[7] nanopolyhedra,[8] and nanostars.[9] To achieve reproducibility of SERS signals, these individual nanostructures could be further fabricated to ordered arrays by self-assembly,[8,10] template method,[11,12] electron beam lithography,[13] or other techniques. Nevertheless, it still remains a challenge to fabricate large-scale uniform substrates with high SERS sensitivity and good signal reproducibility by simple, cost-effective, and green methods.

Nanorods attract considerable attention owing to their anisotropic architecture and multiple LSPR modes.[14,15] Ag nanorod arrays fabricated by oblique angle deposition (OAD) method have been proved to be effective SERS substrates, despite the difficulty to control the gap size between neighboring nanorods and the diameter of nanorods during the OAD preparation.[16] To obtain ordered nanorod arrays, guided OAD has recently been demonstrated.[17] Compared with this method, anodic aluminum oxide (AAO) template-assisted method has been proved to be an easy way to fabricate highly ordered nanorod arrays with controlled gap size and diameter of nanorods.[11] In contrast to the solid nanorods, nanoporous nanorods exhibit additional advantages by their high surface-to-total-volume ratio and bicontinuous nanopores with potentials to create both hot spots and effective

Received: March 24, 2014
Accepted: August 27, 2014
Published: August 27, 2014

 © 2014 American Chemical Society

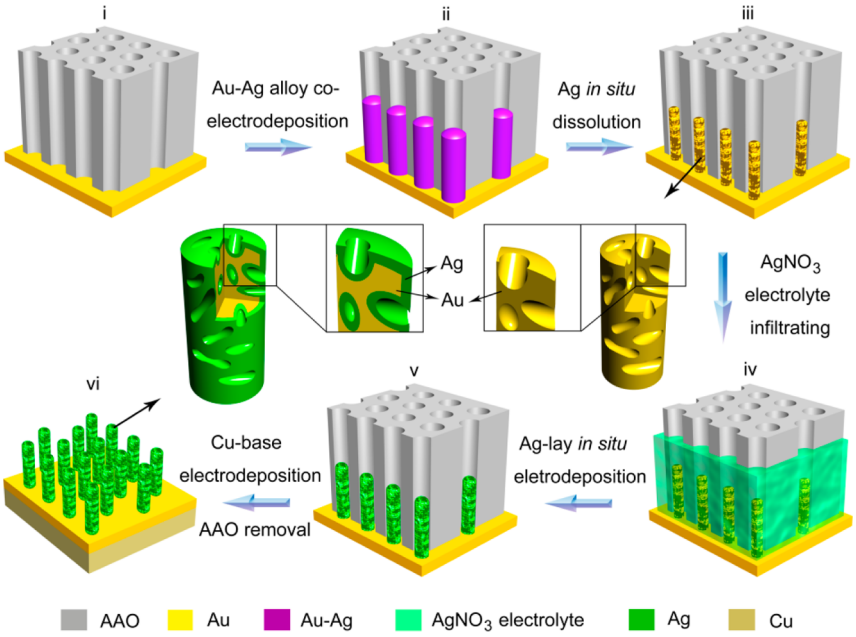

Figure 1. Schematic for the fabrication of core@shell nanoporous Au@Ag nanorod arrays.

adsorbability of the target analyte.[18] It has been demonstrated that the individual nanoporous Au nanorods show notably higher SERS sensitivity than that of the solid Au nanorods.[19] In this respect, if the individual nanoporous Au nanorods are assembled to a large-area and highly ordered arrays, the actual SERS performance would be substantially improved. Recently, nanoporous Au nanorod arrays were tried via the AAO template approach.[20,21] The nanopores were achieved by dealloying of Au−Ag alloy nanorods, which had to be coelectrodeposited by using a cyanide solution containing $KAu(CN)_2$ and $KAg(CN)_2$.[18−22] Although the cyanide solution was extremely toxic, high-cost, and unfriendly to the environment, it was still widely used due to the challenge of finding alternative solutions containing both Au^+ (or Au^{3+}) and Ag^+ for the coelectrodeposition of Au−Ag alloy. Additionally, the fragile nanoporous Au nanorods were easy to bend and connect with each other due to their lack of robust supported base. This random agglomeration and uncontrolled distances between the neighboring nanorods would result in disordered hot spots. For these reasons, little has been reported on the SERS performance of nanoporous Au nanorod arrays.

Herein we present a simple green synthetic approach to large-scale and highly ordered arrays of nanoporous Au nanorods, with an ultrathin Ag-layer coated on the surface of each nanoporous Au nanorod (denoted as core@shell nanoporous Au@Ag nanorod), via a combinatorial process of AAO template-assisted coelectrodepositing Au−Ag alloy nanorods in a new noncyanide electrolyte, in situ dealloying to form nanoporous Au nanorods, in situ electrodepositing an ultrathin Ag-layer on each nanoporous Au nanorod, and subsequently strengthening the bottom Au-layer electrode by electrodepositing a thick Cu-base and then removing the AAO template, as shown schematically in Figure 1. We found a new, cheap, and green electrolyte mainly containing $HAuCl_4$ and $AgNO_3$, to substitute the conventional cyanide solution. As both procedures of dealloying Ag and electrodepositing Ag-layer on the nanoporous Au nanorods were carried out in situ the nanochannels of the AAO template, and the strong Cu-base was electrodeposited to strengthen the arrays before the removal of AAO template, the resultant nanorods remained highly ordered and well-aligned over a large area. The core@shell nanoporous Au@Ag nanorod arrays were proved to be sensitive and reproducible three-dimensional (3D) SERS substrates. Both single-analyte and dual-analytes have been detected by using the SERS substrates, showing great potentials in SERS-based real-time detection.

2. EXPERIMENTAL SECTION

2.1. Materials. Chloroauric acid ($HAuCl_4$), silver nitrate ($AgNO_3$), ethylene diamine tetraacetic acid (EDTA), sodium sulfite (Na_2SO_3), dipotassium hydrogen phosphate trihydrate ($K_2HPO_4{\cdot}3H_2O$), oxalic acid ($H_2C_2O_4$), phosphoric acid (H_3PO_4), copper sulfate pentahydrate ($CuSO_4{\cdot}5H_2O$) and nitric acid (HNO_3) were purchased from Sinopharm Chemical Reagent limited corporation. Rhodamine 6G (R6G) was purchased from Sigma-Aldrich Aurum chlorate. 3,3′,4,4′-Tetrachlorobiphenyl (PCB-77) and 4-Chlorobiphenyl (PCB-3) were purchased from AccuStandard Inc. Milli-Q deionized water (resistivity of 18.2 $M\Omega cm^{-1}$) was used for all preparations. All of the chemicals were used without further purification.

2.2. Fabrication of Core@Shell Nanoporous Au@Ag Nanorod Arrays. The core@shell nanoporous Au@Ag nanorod arrays were fabricated by a porous-AAO template-assisted method. First, the through-pore AAO templates were prepared by a two-step anodization of pure Al foils in $H_2C_2O_4$ (0.3 M) solution under 40 V at 10 °C for 12 h.[23,24] The barrier layer of the resultant AAO templates was removed, and the pores were subsequently widened in H_3PO_4 (5 wt %) solution at 40 °C. An Au-layer (about 200 nm) was ion sputtered onto one side of the AAO template to serve as working electrode.[11] Next, Au−Ag alloy nanorods were coelectrodeposited into the low portions of the AAO-nanochannels under a constant potential at 15 °C for 2−6 min by using a new noncyanide electrolyte; the noncyanide electrolyte was prepared by $HAuCl_4$ and $AgNO_3$ precursor electrolytes, and the $HAuCl_4$ electrolyte was prepared by $HAuCl_4$ (10 g L^{-1}), Na_2SO_3 (160 g L^{-1}), $K_2HPO_4{\cdot}3H_2O$ (30 g L^{-1}), EDTA (5 g L^{-1}), while the $AgNO_3$ electrolyte was prepared by $AgNO_3$ (12 g L^{-1}), Na_2SO_3 (160 g L^{-1}), $K_2HPO_4{\cdot}3H_2O$ (30 g L^{-1}), EDTA (5 g L^{-1}); and the final electrolyte was mixed by $HAuCl_4$ electrolyte and $AgNO_3$ electrolyte according to the ratio of Au^{3+}:Ag^+ (1:2−1:5); the lengths of nanorods were adjusted by tuning the charge passed, and the Au atomic ratio in the Au−Ag alloy nanorods can be effectively tailored by tuning the mole ratio of Au^{3+}:Ag^+ in the noncyanide electrolyte and

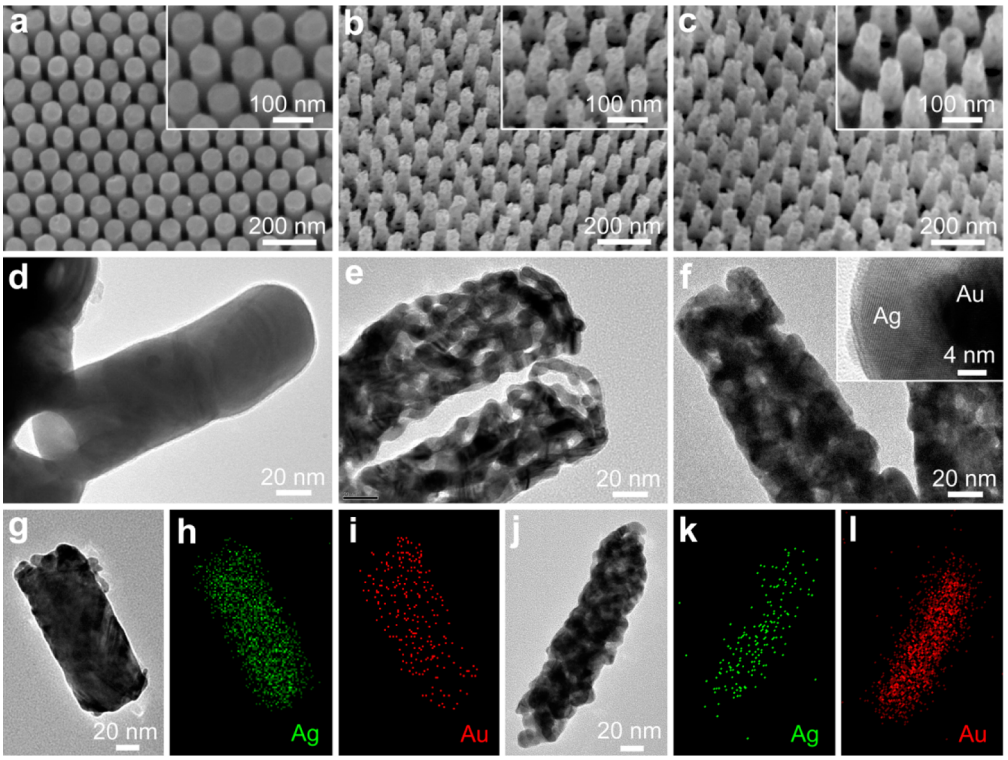

Figure 2. Structural characterizations of the nanorods after different fabrication steps. (a-c) SEM observations and enlarged views (insets) of the solid Au−Ag alloy nanorod arrays, the nanoporous Au nanorod arrays and the core@shell nanoporous Au@Ag nanorod arrays, respectively. (d−f) TEM images of the corresponding individual nanorods shown in (a−c). (g−i) and (j−l) Elemental mappings showing the spatial distribution of Au and Ag in a single solid Au−Ag alloy nanorod and core@shell nanoporous Au@Ag nanorod, respectively.

the electrodeposition potential during the coelectrodeposition process. Next, the nanoporous Au nanorods were achieved by controlled dealloying the as-electrodeposited Au−Ag alloy solid nanorods in situ the AAO-nanochannels, via immerging the whole AAO template in concentrated HNO_3 at 0 °C for only 2 min, followed by thorough rinsing in the deionized water to remove any traces of HNO_3. Then, the arrays of nanoporous Au nanorods within the AAO-nanochannels were used as cathode in the *in situ* Ag-electrodeposition in $AgNO_3$ electrolyte, and an ultrathin Ag-layer was uniformly electrodeposited on both the nanopores and the outer surface of the nanoporous Au nanorods under a constant potential of −0.1 V at 15 °C for 0−30 s, and the thickness of Ag-layer could be tuned by controlling the electrodeposition time. A thick Cu-base (>100 μm) was subsequently electrodeposited on the Au-layer side of the AAO template to strengthen the nanoporous Au@Ag nanorods arrays, using a $CuSO_4$ electrolyte containing $CuSO_4 \cdot 5H_2O$ (160 g L^{-1}) and H_3PO_4 (30 g L^{-1}). Finally, the AAO templates were completely removed via immersing in 5 wt % H_3PO_4, and the core@shell nanoporous Au@Ag nanorod arrays were achieved.

2.3. Characterization. The structure and morphology of the samples were characterized by field-emission scanning electron microscopy (FE-SEM, Sirion 200, Veeco, 10 kV), transmission electron microscopy (TEM, JEM-2010), energy dispersive X-ray spectroscopy (EDS, Oxford). For the UV−vis absorption characterization, the nanorod arrays standing in the AAO templates without the Au-layer electrode and Cu-base were characterized by UV/vis/NIR Spectrophotometer (Cary 5E, Varian, Australia), and the UV−vis spectra of AAO templates were subtracted as baseline.

2.4. SERS Measurement. In the SERS measurement, the as-prepared samples were first treated in Argon plasma for 5 min to eliminate potential contamination. For R6G detection, the substrates were immersed in R6G aqueous solution (1 mL) with varied concentrations for 2 h, followed by thorough rinsing in deionized water to remove the unbound R6G molecules and dried in the air. For the single-analyte detection of polychlorinated biphenyls (PCBs), PCB-77 and PCB-3 were dissolved in acetone with varied concentrations, respectively. Then, the PCBs acetone solutions (10 μL) were dispersed on the as-prepared SERS substrates and dried. To improve the detection sensitivity to PCBs, the substrates were further modified with HS-β-CD, via immersing the samples in 10 g L^{-1} HS-β-CD *N*,*N*-dimethylformamide (DMF) solutions for 8 h, followed by rinsing with DMF and dried. Next, the HS-β-CD-modified substrates were dipped in PCBs acetone solutions (1 mL) for 6 h, rinsed with acetone, and dried. For the dual-analytes detection, the HS-β-CD-modified substrates were completely immersed in R6G/PCBs mixed acetone solutions (with different concentration ratios) and PCB-3/CB-77 mixed acetone solutions for 6 h, respectively, rinsed with acetone, and dried.

All the SERS spectra except for the Raman mappings were measured by using a confocal Raman spectrometer (Renishaw, Invia) equipped with Leica microscope (20× objective lens), and the effective power of the laser source was 0.05 mW for R6G detection, and 0.5 mW for PCBs and mixtures detection. The SERS spectra in Figure 3b were measured with different laser excitation at wavelength of 532, 633, and 785 nm respectively, and all the other were measured with 532 nm laser. The exposure time was 10 s for R6G detection, and 30 s for PCBs and mixtures detection. The Raman mapping was measured by the Renishaw StreamLine accessory with a step size of 1.5 μm and an exposure time of 0.5 s, and other measurement parameters were maintained.

3. RESULTS AND DISCUSSION

3.1. Characterization of Core@Shell Nanoporous Au@Ag Nanorod Arrays. Figure 2 shows the structural characterizations of the nanorod arrays obtained after different fabrication steps. SEM observations reveal the homogeneous morphology of the Au−Ag alloy nanorod arrays (Figure 2a), the nanoporous Au nanorod arrays (Figure 2b), and the core@shell nanoporous Au@Ag nanorod arrays (Figure 2c),

respectively. TEM observations of the corresponding nanorods are shown in Figure 2d−f.

First, highly ordered arrays of hexagonally patterned and vertically aligned Au−Ag alloy solid nanorods (Figure 2a) were achieved after a potentiostatic coelectrodeposition in the new noncyanide electrolyte. The SEM close-up view (inset in Figure 2a) and TEM image (Figure 2d) reveal that the Au−Ag alloy nanorods have a smooth surface, with a predesigned diameter (80 nm) and length (200 nm). The diameters could be tailored by tuning the nanochannel diameter of the AAO template used, while the lengths could be adjusted by controlling the electrical charge passed during the coelectrodeposition. EDS measurement (Figure S1a) shows the nanorods are composed of Ag and Au elements. Elemental mappings (Figure 2g−i) reveal the homogeneous spatial distribution of both Ag and Au elements in the nanorod, implying that the nanorods are composed of Au−Ag alloy, which exhibits similar morphology and structure as those of Au−Ag alloy nanorods fabricated by using the cyanide-based method.[18−22] Thus, the new noncyanide electrolyte is viable for the coelectrodeposition of Au−Ag alloy materials that can be further dealloyed into nanoporous Au. The new electrolyte mainly contains $HAuCl_4$ and $AgNO_3$, in which EDTA, Na_2SO_3, and K_2HPO_4 are added as complex agents that are linked to the Au^{3+} and Ag^+ ions by coordination bonds. By this way, the Au^{3+} and Ag^+ ions could coexist perennially, and no deposit (AgCl) is found in the final electrolyte (crystalline solution). Compared with the conventional cyanide solution, the new electrolyte is cheap, nontoxic, green, and environmental friendly. The cyclic voltammogram (CV) curves for the electrolytes used in Au−Ag alloy, Au, and Ag electrodeposition are shown in Figure S2. The Au and Ag deposition peaks for the Au−Ag alloy are observed at about −0.06 and −0.75 V, respectively. Compared to the cyanide-based method, the Au and Ag deposition potential are lower, implying that the Au and Ag could be electrodeposited more easily.[22] Moreover, our experiments reveal that the higher mole ratio of Au^{3+}:Ag^+ in the electrolyte and the potential in the coelectrodeposition favor higher Au atomic ratio in the resultant Au−Ag alloy nanorods. The detailed experimental results of such a relationship are summarized in Table S1. Therefore, the Au atomic ratio in the Au−Ag alloy nanorods could be effectively tailored by the mole ratio of Au^{3+}:Ag^+ in the electrolyte and the coelectrodeposition potential. As a result, Au−Ag alloy nanorods with Au atomic ratio in the range of 15−35 at. % have been achieved, indicating that the new green electrolyte shows potentials to substitute for the conventional cyanide solution in the coelectrodeposition of Au−Ag alloy.

Then, the nanoporous Au nanorods arrays were achieved by controlled dealloying the as-coelectrodeposited Au−Ag alloy nanorods in situ the AAO-nanochannels with concentrated nitric acid, during which the porous Au architectures form and evolve via a dynamic pattern formation process where the more-noble-metal (Au) atoms tend to aggregate into two-dimensional clusters by phase-separation at the alloy/acid interfaces.[22] Figure 2b shows the array of nanoporous Au nanorods dealloyed from the Au−Ag alloy nanorods with a 26 at. % Au atomic ratio, with the length and diameter about 180 and 60 nm, respectively, being relatively shorter and smaller than the Au−Ag alloy solid nanorods due to the volume shrinkage of the nanorods after Ag dealloying.[25] EDS measurement reveals that nearly all the Ag element has been removed (Figure S1b). Figure 2e clearly reveals the nanoporous features, and the bicontinuous nanopores are formed not only on the outer surface of the nanorods but also inside the nanorods, generating a nanopore diameter of about 13 nm and a ligament size of about 25 nm, respectively. Compared to the solid Au nanorods with a smooth surface (Figure S3), the nanoporous nanorods exhibit additional advantages by their higher surface-to-total-volume ratio and bicontinuous nanopores with potentials to create both hot spots and effective adsorbability of the target analyte. There exists a circular-shaped narrow gap between the resultant nanoporous Au nanorod and the AAO-nanochannel wall due to the volume shrinkage of the nanorods (Figure S4). This gap makes it possible for the $AgNO_3$ electrolyte to infiltrate and immerse the nanoporous Au nanorods for the subsequent Ag-layer electrodeposition to further enhance the SERS sensitivity. Previously nanoporous Au cages or shells were achieved via a galvanic replacement reaction (GRR) method by using $HAuCl_4$ to replace Ag nanoparticles, via a combinatorial process of Ag nanoparticles synthesizing, replacement reacting in $HAuCl_4$ to form Au−Ag alloy shell, and Au−Ag alloy dealloying to form nanoporous Au shell.[26,27] In contrast to the GRR method, our Au−Ag alloy nanorods were achieved by one-step coelectrodeposition, and the nanoporous Au nanorods exhibit a uniform structure inside and outside, and their pore size could be effectively adjusted by controlling the compositions of Au−Ag alloy.

Next, the arrays of nanoporous Au nanorods standing in the AAO-nanochannels were used as cathode in the in situ Ag-electrodeposition, and an ultrathin Ag-layer was electrodeposited on the nanoporous Au nanorods under a constant potential of −0.1 V for 20 s in $AgNO_3$ electrolyte. In comparison with the bare nanoporous Au nanorods (Figure 2b and e), the inner nanopores and the outer surface of each nanoporous Au nanorod were entirely coated with an ultrathin Ag-layer, resulting in an increase in ligament size and a decrease in nanopore size (sub-8 nm, Figure 2c and f). The resultant nanorod still maintained its original nanoporous feature, being indicative of the Ag-layer homogeneity and ultrathin in nature, which is similar to that of the Pt electrodeposition on the ligament surfaces of nanoporous Au.[20] Nanoporous Au has been proved to be excellent substrates for modification of the Pt, Ag, and Ni ultrathin layer.[20,28,29] During the Ag-electrodeposition, the Au core was unchanged due to the physical and chemical stability of Au material, and the electrodeposited Ag-layer was coated on the surface of Au. The Au and Ag were difficult to form alloy at room temperature, therefore it could be suggested that the Au@Ag nanorods possess a core@shell structure. The ultrathin Ag-layer can be identified from the ligament of the nanoporous Au (inset in Figure 2f), and EDS measurement further displays that the Ag element has been electrodeposited (Figure S1c). Elemental mappings (Figure 2j-l) show the electrodeposited Ag element was distributed uniformly in the porous nanorods, therefore the Ag-layer was well-distributed throughout the entire porous network of the nanorods. To provide more convincing evidence for the core@shell structure, thicker Ag-layer was electrodeposited, as shown in Figure S5. In the TEM image of the individual core@shell nanoporous Au@Ag nanorod (Figure S5a), the Ag-layer shell could be identified from the nanoporous Au core, and the corresponding elemental line scanning (Figure S5b) reveals the electrodeposited Ag element is wider than Au, indicating that the resultant nanorods have a core@shell (Au@Ag) structure.

3.2. SERS Sensitivity of Core@Shell Nanoporous Au@Ag Nanorod Arrays. The SERS performance was investigated

by R6G dye as a probe molecule. First of all, the lengths of the nanoporous Au nanorods, the gaps between the neighboring nanoporous Au nanorods, the sizes of the nanopores within the nanoporous Au nanorods, and the thickness of the Ag-layer electrodeposited on the nanoporous Au nanorods, were effectively adjusted to generate the highest SERS signal intensity (see Figure S6−12 in detail). For example, nanoporous Au nanorods with lengths ranging from 50 to 250 nm (Figure S6) were achieved by tuning the electrical charge passed during the coelectrodeposition of Au−Ag alloy nanorods, and their corresponding SERS sensitivities (Figure S7) have also been measured. In general, the SERS intensity not only depends on the EM field enhancement but also depends on the total surface area of the nanostructures. With the increase of nanoporous Au nanorods lengths from 50 to 250 nm, their total surface area continues to increase, while the SERS intensity of the as-prepared substrates improves sharply with the increase of the nanorods lengths from 50 to 180 nm and diminishes for further lengths; thus, the total surface area is not a decisive factor for the improvement of SERS intensity. Our main purpose is to find a substrate with the highest sensitivity (ability to generate the highest signal intensity); therefore, we did not distinguish the total surface area from the EM field enhancement. Similarly, the gaps between the neighboring nanorods, the sizes of the nanopores, and the thickness of the Ag-layer were also effectively adjusted. Taken together, we chose the arrays of nanoporous Au nanorods with lengths about 180 nm, nanorod-gaps about 35 nm, nanopore sizes about 13 nm, and further coated with an ultrathin Ag-layer electrodeposited for 20 s to form core@shell nanoporous Au@Ag nanorod arrays (as shown in Figure 2c) as the optimal SERS substrates in our experiments.

Then, the SERS spectra of R6G with different concentrations adsorbed on the optimal SERS substrates were measured (Figure 3a). The characteristic bands of R6G can be identified clearly even at a concentration as low as 10^{-12} M, demonstrating the high sensitivity of the substrates. The average SERS enhancement factor (EF)[30] of the substrate is estimated to be 1.9×10^8 (Figure S13). Additionally, the SERS spectra of 10^{-6} M R6G adsorbed on the resultant core@shell nanoporous Au@Ag nanorod arrays have also been measured with different excitation wavelength of 532, 633, and 785 nm laser lines, respectively (Figure 3b). It is shown that the 532 nm laser can get stronger signal than those of both 633 and 785 nm laser.

In order to understand the origin of the Raman enhancement, control experiments were performed to distinguish the influence of the nanoporous morphology and the Ag-layer introduced. We compared the LSPR and SERS sensitivities of arrays of core@shell nanoporous Au@Ag nanorods, nanoporous Au nanorods, and solid Au nanorods, all of which have similar sizes with lengths about 180 nm and diameters about 60 nm. In general, there are two LSPR modes for the Au nanorods. One oscillates along the short axis of the nanorods (transverse mode, TM) and is typically in the range of 500−550 nm. The other oscillates along the long axis (longitudinal mode, LM), which is more variable with the plasmon wavelength depending on the sizes of the nanorods, and is typically in the range of 600 nm to near IR.[14,15,18] For the highly ordered arrays of vertically aligned Au nanorods,[31−33] when the incident light was perpendicularly projected on the substrates (at angles of incidence of 0°), the strongest TM could be measured and the LM could hardly be irritated. With the increase of angles of

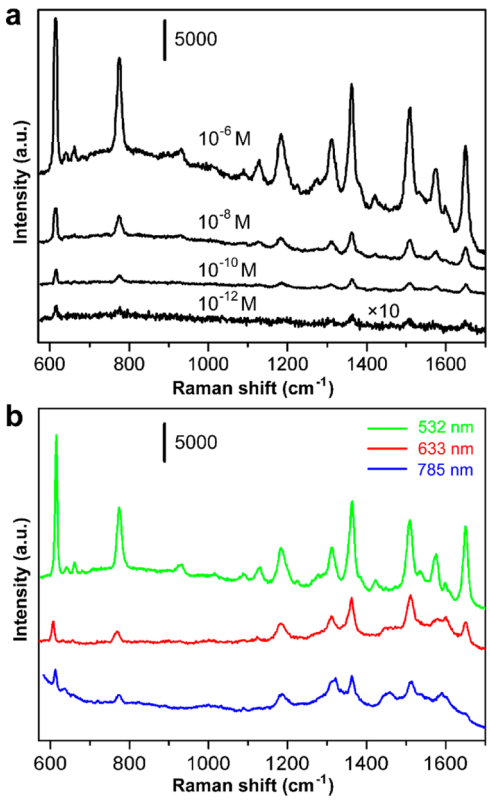

Figure 3. (a) SERS spectra of R6G at varied concentrations (indicated in the upper middle position of each spectrum) collected on the optimal core@shell nanoporous Au@Ag nanorod arrays. (b) SERS spectra of 10^{-6} M R6G adsorbed on the core@shell nanoporous Au@Ag nanorods arrays measured with different excitation wavelength of 532, 633, and 785 nm, respectively.

incidence from 0° to 90°, the TM decreases and the LM increases. To use the TM of the nanorods, we only studied the optical properties as the incident light was perpendicularly projected on the substrates. The UV−vis absorption spectra of arrays of core@shell nanoporous Au@Ag nanorods, nanoporous Au nanorods and solid Au nanorods were characterized, as shown in Figure 4a. For the solid Au nanorods array, the absorption band at 549 nm is observed. For the nanoporous Au nanorods array, the absorption band locates at 558 nm, showing a small red-shift compared to that of the solid nanorods, which is accordant to colloidal solution of nanoporous Au nanorods.[18] After the Ag-layer electrodepositing, the absorption band at 525 nm was observed. All of the bands are near the 532 nm excitation wavelength as we used, which suggests that it is more favorable coupling between the 532 nm excitation wavelength and the plasmonic properties of the above-mentioned structures. Therefore, the SERS sensitivities of core@shell nanoporous Au@Ag nanorods, nanoporous Au nanorods, and solid Au nanorods were compared with the same excitation wavelength of 532 nm, as shown in Figure 4b. For the solid Au nanorod arrays, the SERS effect is ascribed to the EM field enhancement excited by the LSPR coupling between the neighboring nanorods.[11] By contrast, the intensity of R6G bands collected on the nanoporous Au nanorods arrays are about three times as high as those collected on the solid Au nanorod arrays. This big signal enhancement is attributed to the fact that for the nanoporous Au nanorod arrays hot spots are created not only at gaps between the neighboring nanorods but also at large quantities of nanopores within each nanoporous

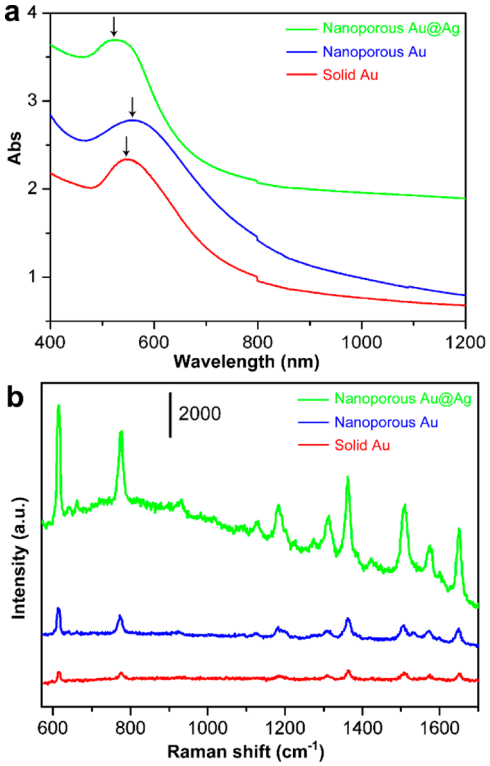

Figure 4. (a) UV−vis absorption spectra of different substrates. (b) SERS spectra of 10^{-8} M R6G adsorbed on the different substrates. From top to bottom in (a) and (b): arrays of core@shell nanoporous Au@Ag nanorods, nanoporous Au nanorods, and solid Au nanorods.

Au nanorod.[19] After electrodepositing the Ag-layer, the signal intensity was further enhanced. On one hand, Ag has a stronger SERS-activity than that of Au and all other materials.[5] On the other hand, it has been demonstrated that the nanoporous Au films with smaller sizes showed stronger enhancements.[34] The thin Ag-layer deposition decreases the size of pores within the nanoporous nanorods from 13 nm (Figure 2e) to sub-8 nm (Figure 2f) level, which is also propitious to the improvement of the SERS sensitivity (see Figures S11 and S12 in detail). Therefore, the ultrathin Ag-layer electrodeposition has a dual-function to further improve their SERS sensitivities. Additionally, the nanoporous Au nanorod arrays also show much higher SERS sensitivity than that of the nanoporous Au films (Figure S14), further demonstrating that the unique 3D structure of the nanoporous Au nanorod arrays exhibits additional advantages in the SERS-based detection.

3.3. SERS Signal Reproducibility of Core@Shell Nanoporous Au@Ag Nanorod Arrays. The SERS signal reproducibility was also tested, as demonstrated by the point-by-point SERS mapping recorded on a randomly selected area (60 μm × 94.5 μm, 40 points × 63 points = 2520 points) of the core@shell nanoporous Au@Ag nanorod arrays by immersing the substrates into 10^{-8} M R6G. As illustrated in Figure 5a, the intensity of the 611 cm^{-1} band from R6G was plotted to demonstrate uniformity across the 3D substrate. To obtain a statistically meaningful result, the intensity distribution of all of the 2520 points is shown in Figure 5b, and the relative standard deviation (RSD) of the intensity is estimated to be 6.5%. Moreover, to assess the substrate-to-substrate reproducibility further, we measured the SERS signals of R6G at 40 randomly chosen spots from 4 samples of core@shell nanoporous Au@Ag nanorod arrays (10 spots per sample), and the RSD of the

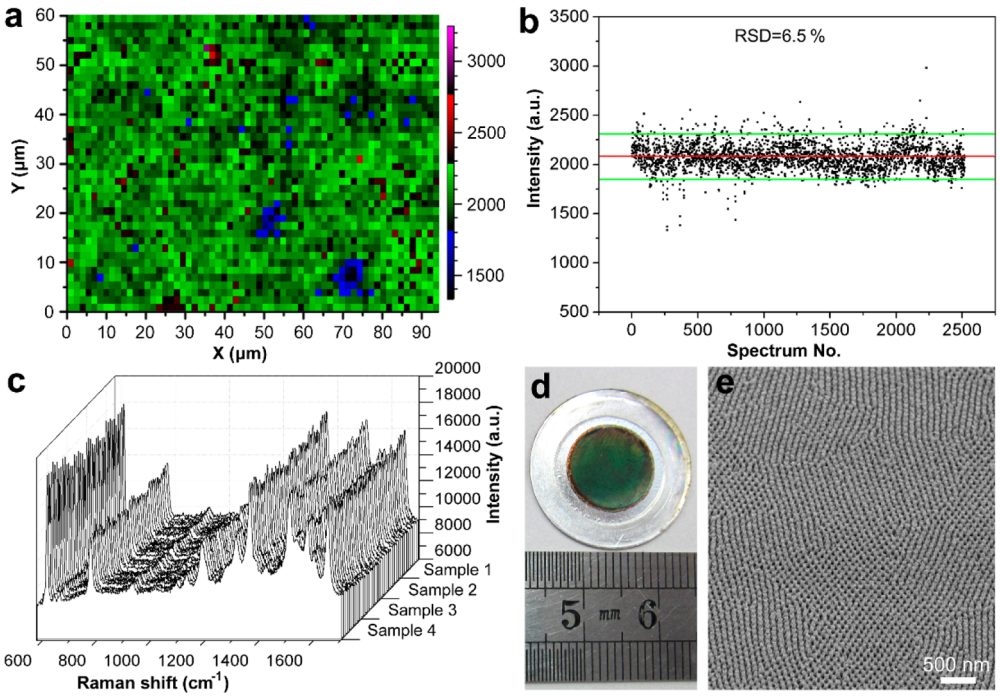

Figure 5. (a) SERS mapping of 611 cm^{-1} peak of R6G adsorbed on the core@shell nanoporous Au@Ag nanorod arrays. (b) Intensity distribution of the 611 cm^{-1} band of the 2520 points in (a). The average intensity is indicated with a red line, and the zones between two green lines represent ±10% intensity variation. (c) SERS spectra of 10^{-7} M R6G obtained at 40 randomly chosen spots from 4 samples of core@shell nanoporous Au@Ag nanorod arrays (10 spots per sample), showing the good substrate-to-substrate reproducibility. (d) Photograph of an intact SERS-substrate of core@shell nanoporous Au@Ag nanorod arrays. (e) Low-magnification SEM image of the core@shell nanoporous Au@Ag nanorod arrays.

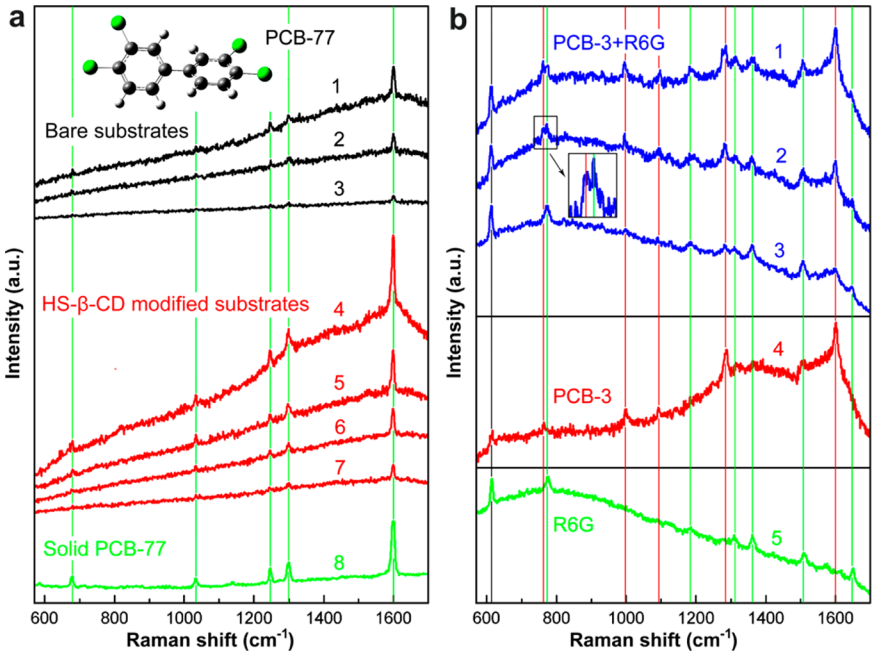

Figure 6. SERS-based single-analyte detection and dual-analytes detection. (a) SERS spectra of PCB-77. Spectra 1−3: 5.35×10^{-4} M, 5.35×10^{-5} M, and 5.35×10^{-6} M PCB-77 adsorbed on the bare core@shell nanoporou Au@Ag nanorod arrays, respectively. Spectra 4−7: 5.35×10^{-4} M, 5.35×10^{-5} M, 5.35×10^{-6} M, and 5.35×10^{-7} M PCB-77 adsorbed on the HS-β-CD-modified core@shell nanoporou Au@Ag nanorod arrays, respectively. Spectrum 8: the normal Raman spectrum of solid PCB-77. (b) Spectra 1−3: SERS spectra of PCB-3 and R6G mixture with concentration (PCB-3:R6G) ratios of 10^{-3} M:10^{-11} M, 10^{-4} M:10^{-11} M, and 10^{-5} M:10^{-11} M adsorbed on the HS-β-CD-modified core@shell nanoporou Au@Ag nanorod arrays. Spectra 4 and 5: pure 1.66×10^{-3} M PCB-3 and 10^{-11} M R6G shown as references.

intensity of the 611 cm^{-1} band from the 40 points is estimated to be 6.8%, as shown in Figure 5c. The homogeneous distribution of the Raman intensity strongly supports the notion that the SERS substrates are uniform in a large area and capable of generating an SERS signal with good reproducibility.

The good signal uniformity can be attributed to our fabrication procedure and the morphological characteristics of the resultant arrays. The AAO template-assisted method has been proved to be an easy way to fabricate highly ordered nanorod arrays with uniform morphologies and controlled sizes.[11,23,24] Most of the procedures in the fabrication of substrates could be continuously accomplished by easy operations and simple devices within a few minutes, and the substrates could be prepared simultaneously within each intact AAO template (>1 cm^2, Figure 5d). Thus, the SERS substrates are easy to fabricate. Furthermore, as the two procedures of dealloying Ag and electrodepositing Ag-layer were both carried out in situ the AAO-nanochannels, the resultant nanorods remained in their original alignement and uniform distribution, being ascribed to the AAO-nanochannel spacial geometrical confinement. In this way, the unique advantage of the highly ordered pore arrangement in AAO template has been more effectively utilized, compared with that of the previously reported AAO template-assisted synthetic approach to nanoporous Au nanorod arrays.[20,21] In addition, prior to the removal of the AAO template, the thick Cu-base (>100 μm) was electrodeposited on the Au-electrode to strengthen the arrays, preventing their destruction and damage in AAO removal and practical applications. As a result, large-area arrays of highly ordered core@shell nanoporous Au@Ag nanorods firmly standing on the bottom Au-layer supported by the Cu-base were achieved, as shown in the low-magnified SEM image (Figure 5e). The large-scale uniformity of the Au−Ag alloy nanorods array and the nanoporous Au nanorods array were also identified in Figures S15a and S15b,c, respectively. The layer-built structures (core@shell nanoporous Au@Ag nanorods, Au-layer and Cu-base) were shown in the cross-sectional SEM images (Figure S15d).

3.4. SERS-Based Single-Analyte and Dual-Analyte Detections of PCBs. Polychlorinated biphenyls (PCBs) belong to one notorious class of persistent organic pollutants (POPs) as defined by the Stockholm Convention,[35,36] and the maximum United States Environmental Protection Agency (USEPA) allowed PCBs contaminant level has been set at 0.00050 mg/L (approximately 10^{-9} M).[37] This concentration could be magnified up to 10^4 times by bioaccumulation.[38] Thus, the rapid trace detection of PCBs is extremely important.[37,39,40] The optimal SERS substrates were further used for a practical trial detection of PCBs. Figure 6a spectra 1−3 shows the SERS spectra of PCB-77 (one congener of PCBs) collected from the substrates of core@shell nanoporous Au@Ag nanorod arrays at concentrations of 5.35×10^{-4}, 5.35×10^{-5}, and 5.35×10^{-6} M, respectively. There are five distinct bands at 678 cm^{-1} (C−Cl stretching), 1033 cm^{-1} (ring breathing), 1246 cm^{-1} (C−H wagging), 1300 cm^{-1} (C−C bridge bond stretching), and 1599 cm^{-1} (ring stretching) in the SERS spectra,[37,39,40] which correspond well with the normal Raman spectrum of solid PCB-77 (spectrum 8 in Figure 6a). Normally, the apolar PCB-77 molecules can be hardly attached to the surface or within the hot spots due to the strong polar nature of noble metal nanostructure interface, also known as nonadsorbing molecules in the SERS-based analysis. However, the large quantities of mouth-open nanopores within each nanorod provide more residence sites for the probe molecules to be adsorbed, demonstrating another unique advantage for SERS-based detection of the apolar molecules. To further reduce the

detection limit of PCBs, we tried to modify the substrates with mono-6-thio-β-cyclodextrin (HS-β-CD), which can easily capture PCBs into its hydrophobic cavity of the β-cyclodextrin,[41] and its chemical structure was shown in Figure S16. After the HS-β-CD was modified, the peak intensities of PCB-77 of the same concentrations were increased significantly (spectra 4−7 in Figure 6a), indicating that HS-β-CD could indeed capture the target PCBs. Now the detection limit is estimated to be 5.35×10^{-7} M, being 1 order of magnitude lower than that of the bare substrates. PCB-3 (another congener of PCBs) has also been identified (Figure S17), showing the SERS substrates have the ability for versatile detection of other PCBs.

For practical detection, real environmental samples usually contain a complex mixture of compounds that need to be quantified. First, it is vital to achieve the target molecule detection under the interference with other background molecules. There are various molecules such as R6G in real samples, which have a low content but generate a strong interference. Therefore, we chose R6G as the impurity to detect PCB-3 at different concentrations, which can imitate the PCBs detection in real environmental samples. By using the HS-β-CD-modified substrates, PCB-3 and R6G mixture with different concentration ratios of 10^{-3} M:10^{-11} M, 10^{-4} M:10^{-11} M, and 10^{-5} M:10^{-11} M were detected, as shown in Figure 6b, spectra 1−3. The vibrational bands of both analytes could be identified clearly, i.e., the 761, 996, 1099, 1287, and 1597 cm^{-1} bands of PCB-3 could be easily distinguished from the 774, 1180, 1311, 1361, 1511, 1575, and 1648 cm^{-1} bands of R6G. It should be noted that the 761 cm^{-1} band of PCB-3 and 774 cm^{-1} band of R6G could be clearly distinguished, even though their wave numbers are so near to each other. Interestingly, the relative intensities correlate well with the analyte concentrations. With the decrease of PCB-3 concentration (from spectrum 1 to spectrum 3 in Figure 6b), the intensities of PCB-3 bands attenuate significantly, while those of R6G bands enhance relatively. As R6G has been widely used as a universal probe molecule in the SERS-based research, the relative intensities of R6G and PCBs bands show potentials to be used in the quantitative detection of PCBs. Second, different congeners of PCBs are always commixed together and difficult to distinguish due to their similar chemical composition and properties. By using the 3D SERS-substrates, the dual-analytes of PCB-77 and PCB-3 in their mixture have also been detected (Figure S18).

4. CONCLUSION

In summary, we have presented a simple green method to Cu-base supported arrays of core@shell nanoporous Au@Ag nanorods. A new, nontoxic, and green electrolyte was found to substitute the conventional cyanide solution. The resultant nanorods remained highly ordered over a large area. As both the nanopores within each nanorod and the gaps between neighboring nanorods created hot spots, the nanoporous Au nanorods arrays exhibited much higher SERS sensitivities than that of the solid Au nanorod arrays, and their SERS sensitivities were further enhanced after the in situ ultrathin Ag-layer electrodeposition. By using the 3D SERS substrates, R6G and PCBs were detected with both high SERS sensitivities and good signal reproducibility. After the HS-β-CD was modified, the detection limit of PCBs was further reduced. Furthermore, mixed solutions of R6G/PCBs and two congeners of PCBs were also identified, showing great potentials in real-time simultaneous detection. Additionally, the proposed AAO template-assisted strategy in combination with noncyanide electrolyte could be developed into a generic simple and green approach to other nanoporous metallic nanorod arrays, such as Pt, Pd, Au, Ag, Cu, and their bimetallic core@shell nanorods, thus opening a door for a wide variety of applications in catalysis, supercapacitors, sensors, and surface wettability.

■ ASSOCIATED CONTENT

Supporting Information

Additional SEM images, EDS spectra, TEM images, Raman spectrum, and SERS spectra. This material is available free of charge via the Internet at http://pubs.acs.org.

■ AUTHOR INFORMATION

Corresponding Author

*E-mail: gwmeng@issp.ac.cn. Fax: (86) 0551-65591434. Tel: (86) 0551-6559274.

Notes

The authors declare no competing financial interest.

■ ACKNOWLEDGMENTS

This work was financially supported by the National Key Basic Research Program of China (Grant 2013CB934304), the CAS/SAFEA International Partnership Program for Creative Research Teams for the financial support, and the NSFC (Grants 11274312 and 21207134).

■ REFERENCES

(1) Li, J. F.; Huang, Y. F.; Ding, Y.; Yang, Z. L.; Li, S. B.; Zhou, X. S.; Fan, F. R.; Zhang, W.; Zhou, Z. Y.; Wu, D. Y.; Ren, B.; Wang, Z. L.; Tian, Z. Q. Shell-Isolated Nanoparticle-Enhanced Raman Spectroscopy. *Nature* **2010**, *464*, 392−395.

(2) Wei, H.; Xu, H. X. Hot Spots in Different Metal Nanostructures for Plasmon-Enhanced Raman Spectroscopy. *Nanoscale* **2013**, *5*, 10794−10805.

(3) Lim, D. K.; Jeon, K. S.; Hwang, J. H.; Kim, H.; Kwon, S.; Suh, Y. D.; Nam, J. M. Highly Uniform and Reproducible Surface-Enhanced Raman Scattering from DNA-Tailorable Nanoparticles with 1-nm Interior Gap. *Nat. Nanotechnol.* **2011**, *6*, 452−460.

(4) Gong, X.; Bao, Y.; Qiu, C.; Jiang, C. Y. Individual Nanostructured Materials: Fabrication and Surface-Enhanced Raman Scattering. *Chem. Commun.* **2012**, *48*, 7003−7018.

(5) Li, W. Y.; Camargo, P. H. C.; Lu, X. M.; Xia, Y. N. Dimers of Silver Nanospheres: Facile Synthesis and Their Use as Hot Spots for Surface-Enhanced Raman Scattering. *Nano Lett.* **2009**, *9*, 485−490.

(6) Osberg, K. D.; Rycenga, M.; Harris, N.; Schmucker, A. L.; Langille, M. R.; Schatz, G. C.; Mirkin, C. A. Dispersible Gold Nanorod Dimers with Sub-5 nm Gaps as Local Amplifiers for Surface-Enhanced Raman Scattering. *Nano Lett.* **2012**, *12*, 3828−3832.

(7) Camargo, P. H. C.; Rycenga, M.; Au, L.; Xia, Y. N. Isolating and Probing the Hot Spot Formed between Two Silver Nanocubes. *Angew. Chem., Int. Ed.* **2009**, *48*, 2180−2184.

(8) Henzie, J.; Grunwald, M.; Widmer-Cooper, A.; Geissler, P. L.; Yang, P. D. Self-assembly of Uniform Polyhedral Silver Nanocrystals into Densest Packings and Exotic Superlattices. *Nat. Mater.* **2012**, *11*, 131−137.

(9) Hao, F.; Nehl, C. L.; Hafner, J. H.; Nordlander, P. Plasmon Resonances of a Gold Nanostar. *Nano Lett.* **2007**, *7*, 729−732.

(10) Cecchini, M. P.; Turek, V. A.; Paget, J.; Kornyshev, A. A.; Edel, J. B. Self-Assembled Nanoparticle Arrays for Multiphase Trace Analyte Detection. *Nat. Mater.* **2013**, *12*, 165−171.

(11) Huang, Z. L.; Meng, G. W.; Huang, Q.; Yang, Y. J.; Zhu, C. H.; Tang, C. L. Improved SERS Performance from Au Nanopillar Arrays by Abridging the Pillar Tip Spacing by Ag Sputtering. *Adv. Mater.* **2010**, *22*, 4136−4139.

(12) Kang, H.; Heo, C. J.; Jeon, H. C.; Lee, S. Y.; Yang, S. M. Durable Plasmonic Cap Arrays on Flexible Substrate with Real-Time Optical Tunability for High-Fidelity SERS Devices. *ACS Appl. Mater. Interfaces* **2013**, *5*, 4569−4574.
(13) Hatab, N. A.; Hsueh, C. H.; Gaddis, A. L.; Retterer, S. T.; Li, J. H.; Eres, G.; Zhang, Z. Y.; Gu, B. H. Free-Standing Optical Gold Bowtie Nanoantenna with Variable Gap Size for Enhanced Raman Spectroscopy. *Nano Lett.* **2010**, *10*, 4952−4955.
(14) Chen, H. J.; Shao, L.; Li, Q.; Wang, J. F. Gold Nanorods and Their Plasmonic Properties. *Chem. Soc. Rev.* **2013**, *42*, 2679−2724.
(15) Kim, S.; Kim, S. K.; Park, S. Bimetallic Gold-Silver Nanorods Produce Multiple Surface Plasmon Bands. *J. Am. Chem. Soc.* **2009**, *131*, 8380−8381.
(16) Driskell, J. D.; Shanmukh, S.; Liu, Y.; Chaney, S. B.; Tang, X. J.; Zhao, Y. P.; Dluhy, R. A. The Use of Aligned Silver Nanorod Arrays Prepared by Oblique Angle Deposition as Surface Enhanced Raman Scattering Substrates. *J. Phys. Chem. C* **2008**, *112*, 895−901.
(17) Keating, M.; Song, S.; Wei, G.; Graham, D.; Chen, Y.; Placido, F. Ordered Silver and Copper Nanorod Arrays for Enhanced Raman Scattering Created via Guided Oblique Angle Deposition on Polymer. *J. Phys. Chem. C* **2014**, *118*, 4878−4884.
(18) Bok, H. M.; Shuford, K. L.; Kim, S.; Kim, S. K.; Park, S. Multiple Surface Plasmon Modes for a Colloidal Solution of Nanoporous Gold Nanorods and Their Comparison to Smooth Gold Nanorods. *Nano Lett.* **2008**, *8*, 2265−2270.
(19) Lee, H. O.; Kim, E. M.; Yu, H.; Jung, J. S.; Chae, W. S. Advanced Porous Gold Nanofibers for Highly Efficient and Stable Molecular Sensing Platforms. *Nanotechnology* **2009**, *20*, 325604.
(20) Yoo, S. H.; Park, S. Platinum-Coated, Nanoporous Gold Nanorod Arrays: Synthesis and Characterization. *Adv. Mater.* **2007**, *19*, 1612−1615.
(21) Gowda, S. R.; Reddy, A. L. M.; Zhan, X. B.; Jafry, H. R.; Ajayan, P. M. 3D Nanoporous Nanowire Current Collectors for Thin Film Microbatteries. *Nano Lett.* **2012**, *12*, 1198−1202.
(22) Ji, C. X.; Searson, P. C. Synthesis and Characterization of Nanoporous Gold Nanowires. *J. Phys. Chem. B* **2003**, *107*, 4494−4499.
(23) Meng, G. W.; Han, F. M.; Zhao, X. L.; Chen, B. S.; Yang, D. C.; Liu, J. X.; Xu, Q. L.; Kong, M. G.; Zhu, X. G.; Jung, Y. J.; Yang, Y. J.; Chu, Z. Q.; Ye, M.; Kar, S.; Vajtai, R.; Ajayan, P. M. A General Synthetic Approach to Interconnected Nanowire/Nanotube and Nanotube/Nanowire/Nanotube Heterojunctions with Branched Topology. *Angew. Chem., Int. Ed.* **2009**, *48*, 7166−7170.
(24) Meng, G. W.; Jung, Y. J.; Cao, A. Y.; Vajtai, R.; Ajayan, P. M. Controlled Fabrication of Hierarchically Branched Nanopores, Nanotubes, and Nanowires. *Proc. Natl. Acad. Sci. U.S.A.* **2005**, *102*, 7074−7078.
(25) Parida, S.; Kramer, D.; Volkert, C. A.; Rosner, H.; Erlebacher, J.; Weissmuller, J. Volume Change During the Formation of Nanoporous Gold by Dealloying. *Phys. Rev. Lett.* **2006**, *97*, 035504.
(26) Song, C. Y.; Abell, J. L.; He, Y. P.; Murph, S. H.; Cui, Y. P.; Zhao, Y. P. Gold-Modified Silver Nanorod Arrays: Growth Dynamics and Improved SERS Properties. *J. Mater. Chem.* **2012**, *22*, 1150−1159.
(27) Sun, Y. G.; Xia, Y. N. Mechanistic Study on the Replacement Reaction between Silver Nanostructures and Chloroauric Acid in Aqueous Medium. *J. Am. Chem. Soc.* **2004**, *126*, 3892−3901.
(28) Huang, J. F. Silver UPD Ultra-Thin Film Modified Nanoporous Gold Electrode with Applications in the Electrochemical Detection of Chloride. *Talanta* **2009**, *77*, 1694−1700.
(29) Huang, J. F. Facile Preparation of an Ultrathin Nickel Film Coated Nanoporous Gold Electrode with the Unique Catalytic Activity to Oxidation of Glucose. *Chem. Commun.* **2009**, 1270−1272.
(30) Le Ru, E. C.; Blackie, E.; Meyer, M.; Etchegoin, P. G. Surface Enhanced Raman Scattering Enhancement Factors: a Comprehensive Study. *J. Phys. Chem. C* **2007**, *111*, 13794−13803.
(31) Evans, P.; Hendren, W. R.; Atkinson, R.; Wurtz, G. A.; Dickson, W.; Zayats, A. V.; Pollard, R. J. Growth and Properties of Gold and Nickel Nanorods in Thin Film Alumina. *Nanotechnology* **2006**, *17*, 5746−5753.
(32) Evans, P. R.; Wurtz, G. A.; Atkinson, R.; Hendren, W.; O'Connor, D.; Dickson, W.; Pollard, R. J.; Zayats, A. V. Plasmonic Core/Shell Nanorod Arrays: Subattoliter Controlled Geometry and Tunable Optical Properties. *J. Phys. Chem. C* **2007**, *111*, 12522−12527.
(33) Wurtz, G. A.; Pollard, R.; Hendren, W.; Wiederrecht, G. P.; Gosztola, D. J.; Podolskiy, V. A.; Zayats, A. V. Designed Ultrafast Optical Nonlinearity in a Plasmonic Nanorod Metamaterial Enhanced by Nonlocality. *Nat. Nanotechnol.* **2011**, *6*, 106−110.
(34) Qian, L. H.; Yan, X. Q.; Fujita, T.; Inoue, A.; Chen, M. W. Surface Enhanced Raman Scattering of Nanoporous Gold: Smaller Pore Sizes Stronger Enhancements. *Appl. Phys. Lett.* **2007**, *90*, 153120.
(35) United Nations Environment Programme. Stockholm Convention on Persistent Organic Pollutants (POPs); 2001; amended in 2009; http://chm.pops.int/.
(36) Sobek, A.; Gustafsson, O. Deep Water Masses and Sediments Are Main Compartments for Polychlorinated Biphenyls in the Arctic Ocean. *Environ. Sci. Technol.* **2014**, *48*, 6719−6725.
(37) Bantz, K. C.; Haynes, C. L. Surface-Enhanced Raman Scattering Detection and Discrimination of Polychlorinated Biphenyls. *Vib. Spectrosc.* **2009**, *50*, 29−35.
(38) Borga, K.; Fisk, A. T.; Hargrave, B.; Hoekstra, P. F.; Swackhamer, D.; Muir, D. C. G. Bioaccumulation Factors for PCBs Revisited. *Environ. Sci. Technol.* **2005**, *39*, 4523−4532.
(39) Zhu, C. H.; Meng, G. W.; Huang, Q.; Zhang, Z.; Xu, Q. L.; Liu, G. Q.; Huang, Z. L.; Chu, Z. Q. Ag Nanosheet-Assembled Micro-Hemispheres as Effective SERS Substrates. *Chem. Commun.* **2011**, *47*, 2709−2711.
(40) Hou, C.; Meng, G. W.; Huang, Q.; Zhu, C. H.; Huang, Z. L.; Chen, B.; Sun, K. X. Ag-Nanoparticle-Decorated Au-Fractal Patterns on Bowl-Like-Dimple Arrays on Al Foil as an Effective SERS Substrate for the Rapid Detection of PCBs. *Chem. Commun.* **2014**, *50*, 569−571.
(41) Wang, J.; Kong, L. T.; Guo, Z.; Xu, J. Y.; Liu, J. H. Synthesis of Novel Decorated One-Dimensional Gold Nanoparticle and Its Application in Ultrasensitive Detection of Insecticide. *J. Mater. Chem.* **2010**, *20*, 5271−5279.